INTERNATIONAL JOURNAL FOR NUMERICAL METHODS IN FLUIDS
Int. J. Numer. Meth. Fluids 2002; **40**:981–998 (DOI: 10.1002/fld.399)

An extended Chebyshev pseudo-spectral benchmark for the 8:1 differentially heated cavity

Shihe Xin[1,2] and Patrick Le Quéré[1,*,†]

[1] *Mechanical Engineering Department, LIMSI-CNRS, BP 133, 91403 Orsay Cedex, France*
[2] *Dépt. de Physique, Univ. Paris Sud, 91405 Orsay Cedex, France*

SUMMARY

Our contribution to the benchmark is multifold. In addition to providing accurate unsteady simulations at the required *Ra* value of 3.4×10^5, we determine accurately the three first critical bifurcation points, investigate the supercritical regime, and study the differences between time-averaged solutions and the corresponding base solution at $Ra = 4 \times 10^5$. We thereby establish the existence of, at least, 4 different branches of solutions and of 3 multiple unsteady periodic solutions for a Rayleigh value of 4×10^5. First appearance of quasi-periodic flow is found at *Ra* about 5.0×10^5 and first appearance of chaotic solutions is found for 5.5×10^5 approximately. We investigate the differences between time-averaged solutions and the corresponding base flow solution at $Ra = 4 \times 10^5$. It is found that they exhibit symmetric feature and similar spatial distribution and that their amplitudes are proportional to the squared amplitude of periodic solutions.
All these computations are carried out using 2D Chebyshev spatial approximations with spatial resolution up to 48×180. For the unsteady computations, a second order time stepping scheme is used, the incompressibility condition being strictly enforced through the use of an influence matrix technique, while for the accurate determination of the critical points, an original algorithm based on a combination of Newton, continuation and Arnoldi Krylov type methods was developed.
Furthermore we investigate the stability of the 2D benchmark solution with respect to 3D periodic disturbances by using a spectral (Chebyshev and Fourier) time-stepping (projection) code. In the 8:1 cavity we did not find any 3D instability before the onset of time dependence of 2D flows nor at the mandatory *Ra* of 3.4×10^5. 3D instabilities were observed for *Ra* about 4×10^5 corresponding to a typical wavelength of two times the cavity width. Copyright © 2002 John Wiley & Sons, Ltd.

KEY WORDS: spectral Chebyshev collocation; unsteady natural convection; time stepping algorithm

1. INTRODUCTION

The motivations of the benchmark and the physical problem have been detailed in Reference [1]. In addition to providing the converged time-averaged solution requested for the benchmark, the present contribution aims at answering some of the additional questions raised in

*Correspondence to: P. Le Quéré, LIMSI-CNRS, B.P. 133, 91403 Orsay Cedex, France.
†E-mail: plq@limsi.fr

Received 31 December 2001
Revised 1 July 2002

Copyright © 2002 John Wiley & Sons, Ltd.

Reference [1]. The main characteristics of the present contribution is that we use spectral Chebyshev collocation for the spatial approximation. This type of approximation is known to provide the best order of convergence in the sense that, unlike methods of *a priori* given finite order, the use of Chebyshev basis expansion provides an approximation whose order of convergence only depends on the regularity of the solution (see References [2, 3]). We use this type of approximation both in the context of time stepping algorithms but also for the direct computation of the steady solutions and of the accurate computation of the critical parameters corresponding to the first three Hopf bifurcation points.

As the benchmark mainly concerns unsteady natural convection flows, numerical integration of the unsteady Navier–Stokes equations (time stepping algorithm) is therefore the cornerstone. Time stepping algorithms, making use of time-schemes to integrate the unsteady Navier–Stokes equations, have long been used to study not only unsteady flows and non-linear dynamics but also the onset of time dependence. When used to study the onset of time dependence, they have some limitations for the following reasons: this methodology is not ideally suited for the accurate determination of the critical value corresponding to the Hopf bifurcation (the accuracy exceeds hardly 3 figures and it will not work at all in the case of a subcritical Hopf bifurcation); further one may miss the most unstable mode if it breaks the symmetry of the base flow solution due to the fact that, although perturbations with the same symmetry as the base flow are naturally triggered by time stepping algorithms, those breaking the symmetry of the base flow have to grow from round-off level which may take very long close to the threshold. Accurate determination of the critical points thus requires algorithms for this specific purpose which have to be used in conjunction with time stepping algorithms.

Linear stability analyses of base flow solutions which do not have an explicit analytical expression consist of two steps: first one should be able to compute the steady base flow solutions, either stable or unstable, a necessary step before investigating the spectrum of their corresponding Jacobian (linearized system). Newton's iteration is the most efficient way to compute the base flow solutions of the steady Navier–Stokes equations while the leading eigenpairs (eigenvalue and eigenfunction) of the Jacobian can be obtained by Arnoldi's method associated with accurate or approximate exponentiation, inverse transformation or continuation method. Newton's iteration however needs most of the time an efficient preconditioning and recent developments have proposed to use a Stokes preconditioning derived from available time stepping algorithms.

In the present contribution, preconditioned Newton's iteration, Arnoldi's method and preconditioned continuation method are combined to determine accurately the transition point corresponding to the onset of time dependence in the benchmark. A time stepping algorithm is also used to obtain accurate unsteady flow fields: the time scheme used is of second-order and the influence matrix technique is used to ensure that the velocity field is divergence free.

Our contribution could stop here had we decided to consider only the two-dimensional aspects of the benchmark. As three-dimensional studies are becoming increasingly more feasible, it seemed interesting to investigate the transition from two-dimensional flow to three-dimensional flow (2D–3D transition). In a companion study [4] we developed a methodology to investigate linear stability analyses of a two-dimensional steady-state base solution with respect to two- and three-dimensional perturbations, which we applied to the present aspect ratio 8 cavity. We assume that the benchmark cavity has infinite depth and that flows are periodic in the direction of cavity depth so that we can use Fourier series. The three-dimensional unsteady Navier–Stokes equations are solved using spectral methods (Chebyshev and Fourier)

Copyright © 2002 John Wiley & Sons, Ltd.

for spatial discretization, a second-order time scheme and a projection method to handle the velocity–pressure coupling. Numerical simulations will be done for a cavity of given depth: if flows are two-dimensional, i.e. invariant by translation in the depth direction, the coefficients of all Fourier modes except the constant mode will turn out to be zero; otherwise flows are three-dimensional and periodic in the depth direction. Since our primary aim is to determine qualitatively the transition points from two- to three-dimensional flows, a time stepping algorithm amply suits for this purpose.

Our contribution is organized as follows. We summarize in the next section the details of the numerical algorithms that were used, we emphasize in particular two-dimensional algorithms for steady-state solving and linear stability analyses and three-dimensional time stepping algorithm. We then present the determination of the critical points, the benchmark results, the optional two-dimensional results of the benchmark and three-dimensional results before giving final conclusions.

2. NUMERICAL METHODS

The two-dimensional results reported here have been obtained entirely by using spectral Chebyshev collocation methods [2, 3]. The velocity components and temperature are sought in polynomial spaces $P_{Nx}(x) \otimes P_{Nz}(z)$. In a Chebyshev collocation method the variables are defined at grid points which are the corresponding Gauss–Lobatto points, i.e.

$$x_i = \left(1 + \cos\left(\frac{\pi i}{Nx}\right)\right)\frac{W}{2} \quad \text{and} \quad z_j = \left(1 + \cos\left(\frac{\pi j}{Nz}\right)\right)\frac{H}{2}$$

with $0 \leqslant i \leqslant Nx$ and $0 \leqslant j \leqslant Nz$. Two different codes have been used: one integrates the two-dimensional unsteady Navier–Stokes equations while the other two were developed more recently to compute directly the steady state solutions and perform linear stability analyses. The three-dimensional results have been obtained by using spectral Chebyshev collocation combined with Fourier Galerkin method. A time stepping projection method has been developed to integrate the three-dimensional unsteady Navier–Stokes equations. In the three codes the Helmholtz equations arising from time discretization are solved by direct diagonalization using eigenvalues and eigenvectors of the second derivative operator [5]. The Lapack library is used to find eigenvalues and eigenvectors, inverse matrices and to perform matrix–matrix and matrix–vector multiplications.

2.1. Two-dimensional time stepping algorithm

The unsteady Navier–Stokes equations are discretized by a second-order time stepping of finite difference type [5]. Non-linear terms in conservative form are treated explicitly, viscous terms are treated implicitly. We use the scheme originally proposed in Reference [6] which combines a BDF2 (see Reference [7]) for the linear part with a second-order Adams Bashforth extrapolation of the convective terms. When applied to a scalar advection–diffusion equation such as

$$\frac{\partial f}{\partial t} + \mathbf{V} \cdot \nabla f = \nabla^2 f$$

Copyright © 2002 John Wiley & Sons, Ltd.

this scheme reads

$$\frac{3f^{n+1}-4f^n+f^{n-1}}{2\Delta t}+2\mathbf{V}\cdot\nabla f^n-\mathbf{V}\cdot\nabla f^{n-1}=\nabla^2 f^{n+1}$$

where Δt is the time step. This equation can be cast in an Helmholtz equation for the unknown field f at time $n+1$:

$$\nabla^2 f^{n+1}-\lambda f^{n+1}=S_f$$

where $\lambda=3/2\Delta t$. The source term S_f of this equation comprises all the known quantities at previous time levels $n\Delta t$ and $(n-1)\Delta t$. As said above, the resulting Helmholtz equation for a scalar field is solved by a direct method based on partial or full diagonalization of the second-order partial derivatives. As for the velocity–pressure coupling, the unsteady Stokes problem is solved exactly at each time step, i.e. both the momentum and continuity equations are enforced simultaneously. This is achieved by an influence matrix or capacitance method [5, 8]. The velocity and pressure fields are sought in polynomial spaces of same order and exactly divergence free solutions are obtained by using the Sherman–Morrison–Woodbury formula [9, 10].

2.2. Two-dimensional steady state and stability analysis algorithm

2.2.1. Governing equations. For the benchmark solution the steady Navier–Stokes equations read in dimensionless form (see Reference [1] for the reference quantities):

$$0=\nabla\cdot\vec{U}$$

$$\frac{\partial\vec{U}}{\partial t}=0=-\nabla P+\frac{Pr}{\sqrt{Ra\,Pr}}\nabla^2\vec{U}+\vec{j}\Theta-\vec{U}\cdot\nabla\vec{U} \tag{1}$$

$$\frac{\partial\Theta}{\partial t}=0=\frac{1}{\sqrt{Ra\,Pr}}\nabla^2\Theta-\vec{U}\cdot\nabla\Theta$$

The stability of $(\vec{U},\Theta,P)$ is governed by the linearized unsteady Navier–Stokes equations for the perturbations $(\vec{u},\theta,p)$:

$$0=\nabla\cdot\vec{u}$$

$$\frac{\partial\vec{u}}{\partial t}=-\nabla p+\frac{Pr}{\sqrt{Ra\,Pr}}\nabla^2\vec{u}+\vec{j}\theta-\vec{U}\cdot\nabla\vec{u}-\vec{u}\cdot\nabla\vec{U} \tag{2}$$

$$\frac{\partial\theta}{\partial t}=\frac{1}{\sqrt{Ra\,Pr}}\nabla^2\theta-\vec{U}\cdot\nabla\theta-\vec{u}\cdot\nabla\Theta$$

If we suppose that $\vec{U}$ and $\vec{u}$ are divergence free, Equations (1) and (2) can be cast into the following form:

$$\frac{\partial\mathbf{X}}{\partial t}=\left(\frac{C}{\sqrt{Ra\,Pr}}L+N\right)\mathbf{X}=0 \tag{3}$$

Copyright © 2002 John Wiley & Sons, Ltd.

and

$$\frac{\partial \mathbf{x}}{\partial t} = \left(\frac{C}{\sqrt{Ra\,Pr}} L + N_{\mathbf{X}} \right) \mathbf{x} = J_{\mathbf{X}} \mathbf{x} \tag{4}$$

where $\mathbf{X} = (\vec{U}, \Theta), \mathbf{x} = (\vec{u}, \theta)$, L representing the two-dimensional Laplace operator—$\nabla^2, N\mathbf{X}$ the remaining terms in equations (1) and $N_{\mathbf{X}}$ the Frechet derivative of N on $\mathbf{X}, J_{\mathbf{X}}$ the Jacobian, $C = 1$ for temperature and $C = Pr$ for velocity.

2.2.2. Steady state solving. The steady-state solver is based on the fact that the steady-state equations and the incremental operator consisting of the difference of the solution between two consecutive time steps have the same solutions [12]. This allows one to use a first-order time stepping scheme (based on explicit treatment for non-linear terms in convective form and implicit for viscous terms) to precondition the steady-state equations (3):

$$\frac{\mathbf{X}^{n+1} - \mathbf{X}^n}{\Delta t} = \frac{C}{\sqrt{Ra\,Pr}} L\mathbf{X}^{n+1} + N\mathbf{X}^n \tag{5}$$

which is equivalent to

$$\frac{\mathbf{X}^{n+1} - \mathbf{X}^n}{\Delta t} = \left(I - \Delta t \frac{C}{\sqrt{Ra\,Pr}} L \right)^{-1} \left(\frac{C}{\sqrt{Ra\,Pr}} L + N \right) \mathbf{X}^n \tag{6}$$

When the same scheme is applied to Equations (4), we obtain similarly:

$$\mathbf{x}^{n+1} = \left(I - \Delta t \frac{C}{\sqrt{Ra\,Pr}} L \right)^{-1} (\Delta t N_{\mathbf{X}} + I) \mathbf{x}^n \tag{7}$$

and

$$\frac{\mathbf{x}^{n+1} - \mathbf{x}^n}{\Delta t} = \left(I - \Delta t \frac{C}{\sqrt{Ra\,Pr}} L \right)^{-1} \left(\frac{C}{\sqrt{Ra\,Pr}} L + N_{\mathbf{X}} \right) \mathbf{x}^n \tag{8}$$

The solution of the non-linear system (3) is obtained through a preconditioned Newton's iteration:

$$\left(I - \frac{C\Delta t}{\sqrt{Ra\,Pr}} L \right)^{-1} \left(\frac{C}{\sqrt{Ra\,Pr}} L + N_{\mathbf{X}} \right) \delta\mathbf{X} = - \left(I - \frac{C\Delta t}{\sqrt{Ra\,Pr}} L \right)^{-1} \left(\frac{C}{\sqrt{Ra\,Pr}} L + N \right) \mathbf{X} \tag{9}$$

$$\mathbf{X} \leftarrow \mathbf{X} + \delta\mathbf{X}$$

and each iteration is solved through matrix free linear solvers such as GMRES [11]. This preconditioning of Newton's iteration is very efficient for large time step.

Note that we have kept so far the factor $C/\sqrt{Ra\,Pr}$ in the preconditioner used so as to be consistant with the governing equations. In practice all equations were multiplied by $\sqrt{Ra\,Pr}/C$ before preconditioning and the preconditioner is then $(I - \Delta t L)^{-1}$. We thus work with $((\sqrt{Ra\,Pr}/C)N + L)\mathbf{X} = 0, (\sqrt{Ra\,Pr}/C)J_{\mathbf{X}}$, etc.

In the steady-state solving algorithm and that for linear stability analysis to be described next the velocity–pressure coupling is enforced through a direct Uzawa method [3] where

Copyright © 2002 John Wiley & Sons, Ltd.

pressure and divergence are only defined and enforced on the inner Gauss–Lobatto points so as not to have spurious pressure modes.

2.2.3. Linear stability analysis by Arnoldi's method. From Equations (8) we have

$$\mathbf{x}^{n+1} = \mathbf{x}^n + \Delta t\left(I - \Delta t\frac{C}{\sqrt{Ra\,Pr}}L\right)^{-1}\left(N_{\mathbf{X}} + \frac{C}{\sqrt{Ra\,Pr}}L\right)\mathbf{x}^n \tag{10}$$

which is an approximate exponential transformation of the Jacobian:

$$\mathbf{x}^{n+1} \approx \mathbf{x}^n + \Delta t\left(N_{\mathbf{X}} + \frac{C}{\sqrt{Ra\,Pr}}L\right)\mathbf{x}^n = \mathbf{x}^n + \Delta t J_{\mathbf{X}}\mathbf{x}^n \approx \exp(\Delta t J_{\mathbf{X}})\mathbf{x}^n$$

for Δt small enough. Since this approximation transforms the eigenvalues of $J_{\mathbf{X}}$ with largest real part into those of largest modulus of $\exp(\Delta t J_{\mathbf{X}})$, we therefore use Arnoldi's method to calculate the leading eigenvalues of $J_{\mathbf{X}}$ (see Reference [12] for details) and to perform the linear stability analysis. The main drawback of this method is that it requires very small Δt and consequently a large number of time steps. It is nevertheless a good method to provide an estimation of the leading eigenvalues and eigenfunctions. In the next subsection we present a method which makes use of this estimation and improves on its accuracy.

2.2.4. Linear stability analysis via continuation. From a linear algebra point of view, the leading eigenvalue $\lambda = \sigma + \mathrm{i}\omega$ and the corresponding discrete eigenfunction $\mathbf{x} = \mathbf{x}^r + \mathrm{i}\mathbf{x}^i$ satisfy the following equations:

$$\begin{aligned} J_{\mathbf{X}}\mathbf{x}^r &= \sigma\mathbf{x}^r - \omega\mathbf{x}^i \\ J_{\mathbf{X}}\mathbf{x}^i &= \sigma\mathbf{x}^i + \omega\mathbf{x}^r \end{aligned} \tag{11}$$

This algebraic system can be solved by Newton's iteration via continuation technique using as initial estimates of λ and $\mathbf{x}$ those obtained with Arnoldi's method. In fact we allow σ and ω to change within Newton's iteration while one component of $\mathbf{x}^r$ and $\mathbf{x}^i$ is normalized. The full process is illustrated below:

$$\begin{vmatrix} J_{\mathbf{X}} - \sigma & \omega & -\mathbf{x}^r & \mathbf{x}^i \\ -\omega & J_{\mathbf{X}} - \sigma & -\mathbf{x}^i & -\mathbf{x}^r \\ \mathbf{e}_l^T & 0 & 0 & 0 \\ 0 & \mathbf{e}_l^T & 0 & 0 \end{vmatrix} \begin{vmatrix} \delta\mathbf{x}^r \\ \delta\mathbf{x}^i \\ \delta\sigma \\ \delta\omega \end{vmatrix} = - \begin{vmatrix} J_{\mathbf{X}}\mathbf{x}^r - \sigma\mathbf{x}^r + \omega\mathbf{x}^i \\ J_{\mathbf{X}}\mathbf{x}^i - \sigma\mathbf{x}^i - \omega\mathbf{x}^r \\ 0 \\ 0 \end{vmatrix}$$

$$\begin{aligned} \mathbf{x}^r &\leftarrow \mathbf{x}^r + \delta\mathbf{x}^r \\ \mathbf{x}^i &\leftarrow \mathbf{x}^i + \delta\mathbf{x}^i \\ \sigma &\leftarrow \sigma + \delta\sigma \\ \omega &\leftarrow \omega + \delta\omega \end{aligned} \tag{12}$$

where $\mathbf{e}_l^{\mathrm{T}}$ is the transpose of the lth unit vector $\mathbf{e}_l$ and l should correspond to an ordinary point, i.e. one interior point. Equations (12) are first multiplied by $\sqrt{Ra\,Pr}/C$, then preconditioned

Copyright © 2002 John Wiley & Sons, Ltd.

by discrete Stokes operator $(I - \Delta t L)^{-1}$ and finally solved again by GMRES in the same manner as Equation (9).

This method was initially proposed by Chenier [13] to better follow the eigenpair λ and $\mathbf{x}$. It is more powerful than just following the eigenpair and improving the accuracy. For the linear stability analysis we are not only interested in the value of λ corresponding to a given value of Rayleigh number but, more importantly, in the value of Rayleigh number at which λ becomes of zero real part, i.e. the critical Rayleigh number. This is another search of root of $\sigma(Ra) = 0$ which can be performed with secant method coupled with Equations (9) and (12). The entire search process was made fully automatic and can be summarized as follows:

1. Fix Ra_1 and solve Equation (9) to obtain the corresponding $\mathbf{X}_1$
2. Use Arnoldi's method to find the leading eigenpairs λ and $\mathbf{x}$
3. Choose one eigenpair and solve Equations (12) so as to determine accurately $\lambda_1 = \sigma_1 + \mathrm{i}\omega_1$
4. Prescribe a ΔRa, set $Ra_2 = Ra_1 - \mathrm{sign}(\sigma_1)\Delta Ra$ and solve Equation (9) and then Equations (12) to obtain $\mathbf{X}_2$ and $\lambda_2 = \sigma_2 + \mathrm{i}\omega_2$
5. Set $Ra_3 = Ra_1 - (Ra_2 - Ra_1) \times \sigma_1/(\sigma_2 - \sigma_1)$, solve again Equation (9) and Equation (12) to find $\mathbf{X}_3$ and $\lambda_3 = \sigma_3 + \mathrm{i}\omega_3$
6. If $|\sigma_3| < \varepsilon$ go to Step 7, otherwise compare the sign and the magnitude of σ_3 with those of σ_1 and σ_2, assign the results of previous step to either set 1 (Step 3) or set 2 (Step 4) and repeat Step 5 until the convergence criterion is satisfied.
7. Go back to Step 3 with another eigenpair if there is any, otherwise stop.

The algorithm for steady-state solving and linear stability analysis has been applied successfully to a circular differentially heated cavity [14] and a differentially heated square cavity with conducting horizontal walls [4]. More details can be found in References [12, 13, 15–18].

2.3. Three-dimensional time stepping algorithm

The three-dimensional unsteady Navier–Stokes equations of the benchmark problem are discretized in time by using the same second-order scheme as for the two-dimensional case. Note that non-linear terms are in convective form rather than conservative form. The discretized equations read then

$$
\begin{aligned}
0 &= \nabla \cdot \vec{u}^{n+1} \\
\frac{3\vec{u}^{n+1} - 4\vec{u}^{n} + \vec{u}^{n-1}}{2\Delta t} + 2(\vec{u} \cdot \nabla \vec{u})^{n} - (\vec{u} \cdot \nabla \vec{u})^{n-1} &= -\nabla p^{n+1} + \frac{Pr}{\sqrt{Ra\,Pr}} \nabla^2 \vec{u}^{n+1} + \vec{j}\theta^{n+1} \\
\frac{3\theta^{n+1} - 4\theta^{n} + \theta^{n-1}}{2\Delta t} + 2(\vec{u} \cdot \nabla \theta)^{n} - (\vec{u} \cdot \nabla \theta)^{n-1} &= \frac{1}{\sqrt{Ra\,Pr}} \nabla^2 \theta^{n+1}
\end{aligned}
\tag{13}
$$

Although the influence matrix technique or direct Uzawa method could be used to enforce the velocity–pressure coupling in the case of two Chebyshev and one Fourier directions, we choose to use a projection method consisting of two steps. In the first step (prediction) we solve the momentum and energy equations by dropping the divergence-free condition and

Copyright © 2002 John Wiley & Sons, Ltd.

using the pressure p^n at time step n:

$$\begin{aligned}
&\frac{3\theta^{n+1}-4\theta^n+\theta^{n-1}}{2\Delta t}+2(\vec{u}\cdot\nabla\theta)^n-(\vec{u}\cdot\nabla\theta)^{n-1}=\frac{1}{\sqrt{Ra\,Pr}}\nabla^2\theta^{n+1}\\
&\frac{3\vec{u}^*-4\vec{u}^n+\vec{u}^{n-1}}{2\Delta t}+2(\vec{u}\cdot\nabla\vec{u})^n-(\vec{u}\cdot\nabla\vec{u})^{n-1}=-\nabla p^n+\frac{Pr}{\sqrt{Ra\,Pr}}\nabla^2\vec{u}^*+\vec{j}\theta^{n+1}
\end{aligned} \tag{14}$$

The corresponding boundary conditions are those of θ^{n+1} and $\vec{u}^{n+1}$.

As $\vec{u}^*$ is not divergence free, the second step consists of its projection on the divergence free subspace by solving the following system:

$$\frac{3(\vec{u}^{n+1}-\vec{u}^*)}{2\Delta t}=-\nabla(p^{n+1}-p^n)$$

coupled with $\nabla\cdot\vec{u}^{n+1}=0$. This can be done by solving

$$\frac{3\nabla\cdot\vec{u}^*}{2\Delta t}=\nabla\cdot\bar{I}\nabla(p^{n+1}-p^n) \tag{15}$$

where $\bar{I}$ is a modified identity matrix whose first and last diagonal elements are zero to account for the fact that $\vec{u}^{n+1}=\vec{u}^*$ on the boundaries. After solving Equation (15), $\vec{u}^{n+1}$ is explicitly recovered by

$$\vec{u}^{n+1}=\vec{u}^*-\frac{2\Delta t}{3}\nabla(p^{n+1}-p^n)$$

and the pressure is incremented. More details on numerical analysis of projection method can be found in Reference [19].

3. NUMERICAL RESULTS

The results presented in this section are mainly two-dimensional. Three-dimensional results are presented in Section 3.4. It is to be noted that the results presented are all dimensionless and based on the reference quantities [1].

The symmetry properties of the two-dimensional solutions, recalled in Reference [1], are the following:

$$(\Theta,\vec{U},P)(x,y)=-(\Theta,\vec{U},-P)(W-x,H-y)$$

A solution possessing this symmetry exhibits skew-symmetry in the velocity and temperature fields, and will be defined as the 'skew-symmetric' (SS). It is known that the eigenmodes will have either the same symmetry or the opposite one, i.e.

$$(\tilde{\theta},\tilde{u},\tilde{v},\tilde{p})(x,y)=-(\tilde{\theta},\tilde{u},\tilde{v},-\tilde{p})(W-x,H-y)$$

or

$$(\tilde{\theta},\tilde{u},\tilde{v},\tilde{p})(x,y)=(\tilde{\theta},\tilde{u},\tilde{v},-\tilde{p})(W-x,H-y)$$

The eigenmodes breaking the base flow symmetry will be called symmetry-breaking (SB) [1].

Copyright © 2002 John Wiley & Sons, Ltd.

Table I. Critical points of the first three modes. Ra_c—critical Rayleigh number, ω_c—critical angular frequency, $\mathscr{T}_c$—critical period, SS—skew-symmetric and SB—symmetry-breaking.

Spatial resolution $Nx \times Nz$	32×120	40×140
Mode 1		
Ra_c	306180.6	306191.6
ω_c	1.7090808	1.7090841
$\mathscr{T}_c$	3.6763536	3.6763464
Symmetry	SB	SB
Mode 2		
Ra_c	311164.6	311169.8
ω_c	1.8349142	1.8349204
$\mathscr{T}_c$	3.4242394	3.4242277
Symmetry	SS	SS
Mode 3		
Ra_c	333899.6	
ω_c	1.9661282	
$\mathscr{T}_c$	3.1957149	
Symmetry	SB	

3.1. Critical points

The accurate determination of the first critical points has been carried out by using the methodology described above. A steady solution at a given Rayleigh number is obtained using the steady-state solver. Its linear stability is then investigated by Arnoldi's method. The largest real part of the leading eigenvalues indicates whether the Rayleigh number investigated is supercritical and provides an estimate of its distance from the critical point. By adjusting the Rayleigh number according to the sign and the value of the largest real part of the leading eigenvalues, we are able to approach the critical points, i.e. determine a Rayleigh number at which the largest real part of the leading eigenvalues is in the neighbourhood of 0. The steady-state base solution and the eigenpairs provided by Arnoldi's method are then used as initial guesses for the search of the bifurcation point by secant method: Equations (12) and (9) are solved to implement the secant method solving $\sigma(Ra) = 0$.

The critical points of the first three unstable modes were thus computed. Two spatial resolutions are used for the first two modes to give an indication of the spatial convergence of the results. Critical Rayleigh numbers, critical angular frequencies and the symmetries of the corresponding unstable modes are summarized in Table I. The corresponding spatial structures of the temperature component of the eigenmodes are displayed in Plate 1.

These results were obtained with the following convergence or stopping criteria. For steady-state the iterative procedure was stopped when the $\|\cdot\|_\infty$ of the correction became smaller than 10^{-7}. In the refinement of the leading eigenpairs, Newton's iteration was stopped when the correction's $\|\cdot\|_\infty < 10^{-9}$ and the critical points are considered to be found when $|\mathscr{R}(\lambda)| < 10^{-6}$ and the corresponding correction on Rayleigh number is then less than 0.2.

Copyright © 2002 John Wiley & Sons, Ltd.

The most unstable mode (Mode 1) was found to be symmetry-breaking and thus has the opposite symmetry of the base flow solution while the second most unstable mode (Mode 2) keeps this symmetry and Mode 3 breaks again the symmetry of the base flow solution. If one considers two successive patches of the eigenmode, one positive and one negative, as one wave structure, it can be seen that Mode 1 consists of 10 wave structures, Mode 2 of 11 structures and Mode 3 of 12 structures.[‡] These structures travel clockwise around the cavity, in the direction of the primary circulation, and the fact that the eigenmodes have their maximum amplitudes along the side walls indicates that it is a boundary layer type instability. Computations were first realized using a spatial resolution of $Nx \times Ny = 32 \times 120$ which is thought to be high enough to get accurate results according to classical scaling laws and from previous experience. A higher resolution of 40×140 was however used to confirm these values (Mode 1 and Mode 2). The comparison shows that the maximum difference occurs for the critical Rayleigh numbers: an absolute difference of 11 in Ra_c for Mode 1, which corresponds to a relative difference of 0.0033%, is observed. Spatial convergence can thus be considered as obtained.

3.2. *Time-dependent solution at* $Ra = 3.4 \times 10^5$

Although multiple solutions have been found at supercritical Rayleigh numbers (see next section), it seems that there is only one periodic solution at $Ra = 3.4 \times 10^5$. Two spatial resolutions of $Nx \times Ny = 32 \times 120$ and 48×180 have been used to perform numerical simulations. We first used a spatial resolution of $Nx \times Ny = 32 \times 120$ to investigate the problem. Once the finite amplitude time-periodic solution was obtained, the solution was interpolated to a finer spatial resolution of 48×180 and time integration was resumed. A comparison showed that the solution for spatial resolution 48×180 can be considered as fully converged. A detailed examination of the flow structures shows that unsteady flow at this mandatory Rayleigh number issues from the second most unstable mode (Mode 2) and keeps the base flow symmetry. Both the pointwise and global quantities required for the benchmark are presented in Table II for spatial resolution 48×180 and several time step values to show the convergence. It is noted that the period of unsteady nonlinear solution is equal to 3.4115 and that it is very close to the critical period of Mode 2 at the bifurcation point ($\mathscr{T}_c = 3.4242$).

3.3. *Additional two-dimensional results*

In this section we present extended two-dimensional results obtained for the benchmark problem: flow regime, unstable base solution and time-averaged solutions at supercritical Ra.

3.3.1. Flow regime at supercritical Ra. We investigated a range of Rayleigh values from Ra_c to 6×10^5 to identify the various branches of solutions and to get an indication of the first appearance of chaos. What happens in this range is very similar to what was already observed in cavities of other aspect ratio [20].

Figure 1 summarizes dozens of hours of computing time. Starting from a slightly supercritical Rayleigh number, and increasing Ra by small increments, asymptotic periodic solutions

[‡]It is easy to see that modes that have the base flow symmetry have an odd number of wave structures while modes with an even number of wave structures break the symmetry.

Copyright © 2002 John Wiley & Sons, Ltd.

Table II. Local and global results at $Ra = 3.4 \times 10^5$. Nu_c represents the centerline Nusselt number, i.e. dimensionless heat flux across the cavity centreline.

	Grid resolution: 48×180 Time duration: 3900 Steps per period: 404.87			Grid resolution: 48×180 Time duration: 1000 Steps per period: 809.74		
Quantity	Average	Amplitude	Period	Average	Amplitude	Period
u_1	5.6356×10^{-2}	5.4829×10^{-2}	3.4115	5.6348×10^{-2}	5.4782×10^{-2}	3.4115
v_1	0.46188	7.7206×10^{-2}	3.4115	0.46188	7.7143×10^{-2}	3.4115
θ_1	0.26548	4.2735×10^{-2}	3.4115	0.26548	4.2700×10^{-2}	3.4115
Skewness	0	0		0	0	
ΔP_{14}	-1.8548×10^{-3}	2.0380×10^{-2}	3.4115	-1.8536×10^{-3}	2.0361×10^{-2}	3.4115
ΔP_{51}	−0.53486	2.2466×10^{-2}	3.4115	−0.53486	2.2447×10^{-2}	3.4115
ΔP_{35}	0.53671	1.0067×10^{-2}	3.4115	0.53671	1.0059×10^{-2}	3.4115
Nu_0	−4.57946	7.0995×10^{-3}	3.4115	−4.57946	7.0936×10^{-3}	3.4115
Nu_c	−4.57946	0.17777	3.4115	−4.57946	0.17765	3.4115
Nu_W	−4.57946	7.0995×10^{-3}	3.4115	−4.57946	7.0936×10^{-3}	3.4115

	Grid resolution: 48×180 Time duration: 700 Steps per period: 2024.37			Grid resolution: 48×180 Time duration: 400 Steps per period: 4048.75		
Quantity	Average	Amplitude	Period	Average	Amplitude	Period
u_1	5.6345×10^{-2}	5.4768×10^{-2}	3.4115	5.6345×10^{-2}	5.4767×10^{-2}	3.4115
v_1	0.46188	7.7125×10^{-2}	3.4115	0.46188	7.7123×10^{-2}	3.4115
θ_1	0.26548	4.2690×10^{-2}	3.4115	0.26548	4.2689×10^{-2}	3.4115
Skewness	0	0		0	0	
ΔP_{14}	-1.8536×10^{-3}	2.0355×10^{-2}	3.4115	-1.8536×10^{-3}	2.0355×10^{-2}	3.4115
ΔP_{51}	−0.53486	2.2442×10^{-2}	3.4115	−0.53486	2.2441×10^{-2}	3.4115
ΔP_{35}	0.53671	1.0057×10^{-2}	3.4115	0.53671	1.0056×10^{-2}	3.4115
Nu_0	−4.57946	7.0921×10^{-2}	3.4115	−4.57946	7.0918×10^{-3}	3.4115
Nu_c	−4.57946	0.17761	3.4115	−4.57946	0.17761	3.4115
Nu_W	−4.57946	7.0921×10^{-3}	3.4115	−4.57946	7.0918×10^{-3}	3.4115

were obtained after the transients following the sudden change in Ra decayed. These solutions consist of 10 wave structures and oscillate with the critical period ($\mathscr{T} = 3.6764$). The symmetry of the base flow solution is broken. Solutions possessing the same characteristics have been obtained up to $Ra = 3.2 \times 10^5$ and this is the first branch of unsteady solutions. Using a periodic solution at $Ra = 3.2 \times 10^5$ as initial condition, Ra was then increased to 3.3×10^5. After a long transient (Figure 2) a periodic solution of finite amplitude is finally obtained, with an oscillating period of 3.42. A close examination of the fluctuations shows that they are symmetric: the base solution symmetry is restored and the periodic solution is induced by the second most unstable mode (Mode 2 : 11 wave structures). From this periodic solution Ra was further increased or decreased and periodic solutions of the same structure have been

Copyright © 2002 John Wiley & Sons, Ltd.

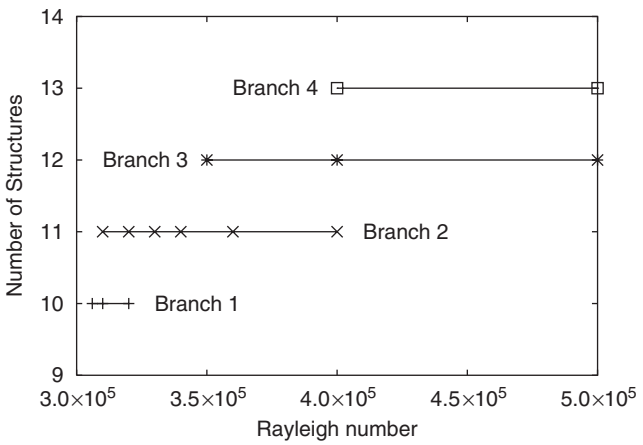

Figure 1. Multiple solution diagram.

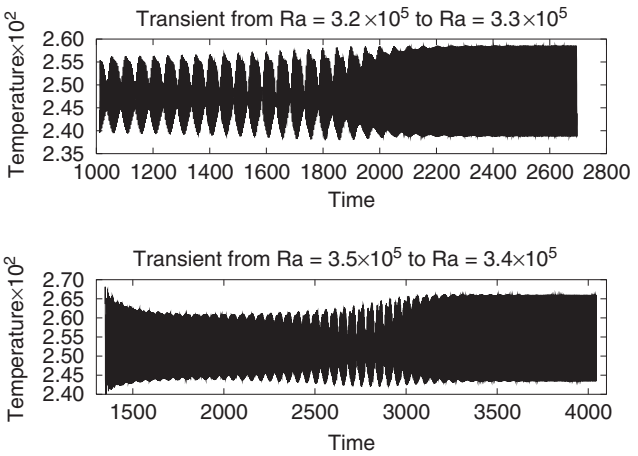

Figure 2. Time evolutions of transients between solution branches.

obtained up to $Ra = 4 \times 10^5$ and down to $Ra = 3.12 \times 10^5$. This is the second branch of unsteady solutions, whose ending point is located around $Ra = 4.1 \times 10^5$. Note already that for $Ra = 3.15 \times 10^5$ there are two possible solutions to the unsteady Navier–Stokes equations. In the same way the third and fourth branches of unsteady solutions were obtained: on the third branch solutions are symmetry-breaking (Mode 3) and have 12 wave structures (breaking the symmetry of base solution) and solutions on the fourth are symmetric and have 13 wave structures (preserving the symmetry of base flow solution). The third solution branch ranges approximately from $Ra = 3.5 \times 10^5$ to $Ra = 5.7 \times 10^5$. The lower value was determined from Figure 2 which displays the transient from $Ra = 3.5 \times 10^5$ to 3.4×10^5—from Branch 3 to Branch 2. The starting point of the fourth branch was located around 3.9×10^5. Note also that at $Ra = 4 \times 10^5$ three different periodic solutions were found, all of which remained stable

Copyright © 2002 John Wiley & Sons, Ltd.

Table III. Maxima of the differences between time-averaged and unstable base solution at $Ra = 4 \times 10^5$.

	Branch 2	Branch 3	Branch 4
u	3.6669×10^{-2}	3.3154×10^{-2}	1.6191×10^{-2}
v	3.9079×10^{-2}	3.5327×10^{-2}	1.6770×10^{-2}
θ	9.6237×10^{-3}	8.8987×10^{-3}	4.0563×10^{-3}

over thousands of dimensionless time units, which of course does not constitute a definitive proof of their stability. Surprisingly (and fortunately) enough, for the mandatory value of $Ra = 3.4 \times 10^5$ of the benchmark, there thus seems to exist only one periodic solution.

We did not perform more detailed computations to investigate the stability limits of each solution branch because of the difficulties in finding these limits: to the best of our methodology they can only be determined by working with infinitesimal perturbations, which means using very small increments of Rayleigh number and integrating for long computing times; it is noted that the transients get longer and richer[§] when approaching these limits and the computations are consequently very expensive. These figures should still be considered as indicative in the sense that the limits of each branch remain to be accurately determined.

On the first two branches unsteady solutions are periodic (apart from the previous remarks) while on the third and fourth we observed transition to quasi-periodicity and to chaos: the first appearance of quasi-periodic solutions was observed for $Ra = 5.4 \times 10^5$ on the third branch and $Ra = 5.0 \times 10^5$ on the fourth branch; The appearance of chaos occurred for $Ra = 5.7 \times 10^5$ on the third branch and $Ra = 5.5 \times 10^5$ on the fourth branch.

3.3.2. Time-averaged and unstable steady-state solutions at supercritical Ra. When flows in the cavity become unsteady, the time-averaged solutions differ from the corresponding unstable base flow solution and it is interesting to investigate their difference (see the benchmark proposal [1]). As we have access to both unstable steady-state solutions and time-averaged solutions, we computed and tried to interpret the difference. We chose to do this at a Rayleigh number of 4×10^5 for which there are three different periodic (and hence three different time-averaged) solutions. Each periodic solution stems from a different pair of complex linearly unstable modes of the Jacobian which correspond to the three modes shown in Plate 1. In Plate 2 are plotted the differences between the time-averaged and unstable steady-state solutions for the three branches. These differences seem to be symmetric and their spatial distributions are very similar (almost the same pattern). They are however not the same and their corresponding maxima are given in Table III showing that the difference of largest amplitude corresponds to Branch 2 and that of smallest amplitude to Branch 4. It seems therefore that at $Ra = 4 \times 10^5$ different branches of periodic solutions give rise, in a time-average sense, to different deviations from the corresponding unstable steady-state solution but they seem to have little effect on the symmetry of the deviations.

[§]It is possible to observe quasi-periodic flows in the vicinity of the branch limits before unsteady solutions change branch. Unsteady solutions later referred to as first quasi-periodic flows are not to be confused with these quasi-periodic flows observed in the vicinity of the branch limits.

Copyright © 2002 John Wiley & Sons, Ltd.

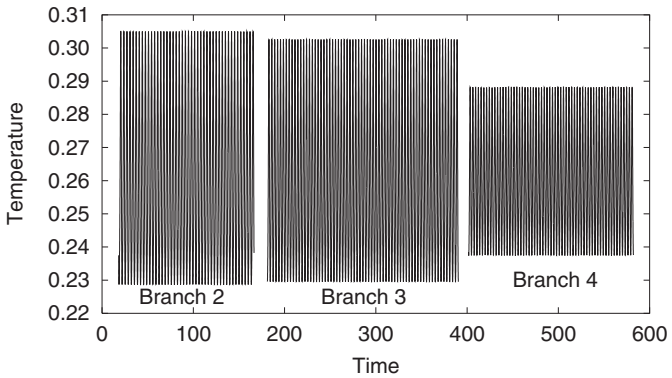

Figure 3. Periodic solutions at $Ra = 4 \times 10^5$. The corresponding amplitudes are equal to 0.0763351, 0.0729947 and 0.0507559, respectively, for Branch 2, Branch 3 and Branch 4. The ratios between the amplitudes squared are in close agreement with those between the maxima listed in Table III.

In the vicinity of the corresponding bifurcation point, one can consider $\sqrt{Ra - Ra_c}$ as a small parameter and expand the full saturated (finite-amplitude) non linear unsteady solution into a polynomial series of $\varepsilon = \sqrt{Ra - Ra_c}$ i.e. $\sum_{n=0} \mathbf{x}^{(n)} \varepsilon^n$. For $n = 0, \mathbf{x}^{(0)}$ is chosen to be the base solution $\mathbf{X}$; for $n = 1, \mathbf{x}^{(1)}$ is the pair of complex unstable modes, which oscillates in time as $\exp(\pm i\omega t)$ and is governed by the linearized N–S equations. The time-average of $\mathbf{x}^{(1)}, \overline{\mathbf{x}^{(1)}}$, is therefore equal to zero. For $n = 2$, the governing equations are the following:

$$\frac{\partial \mathbf{x}^{(2)}}{\partial t} = \left(\frac{C}{\sqrt{Ra\,Pr}} L + N_{\mathbf{x}^{(0)}} \right) \mathbf{x}^{(2)} - \tilde{N}\mathbf{x}^{(1)} \tag{16}$$

where $\tilde{N}\mathbf{x}^{(1)}$ represents the full non-linear terms. It is noted that, whatever the symmetry of $\mathbf{x}^{(1)}, \tilde{N}\mathbf{x}^{(1)}$ is always symmetric, and $\mathbf{x}^{(2)}$ is therefore symmetric. The non linear interaction of $\mathbf{x}^{(1)}$ with itself, i.e. $\tilde{N}\mathbf{x}^{(1)}$, yield a time-independent part and a time-periodic part oscillating like $\exp(\pm 2i\omega t)$. $\overline{\mathbf{x}^{(2)}}$, the time-average of $\mathbf{x}^{(2)}$, is thus different from zero and contributes to leading order to the difference between the time-averaged and base flow solution. This explains why the differences between the time-averaged and unstable steady-state solutions are all seemingly symmetric, although strictly speaking only those corresponding to branches 2 and 4 (eigenmodes which have the base flow symmetry) should have this property.

The above analyses also show that deviations of time-average from base solution are proportional to the amplitude squared of $\mathbf{x}^{(1)}$. Figure 3 displays time-evolutions of temperature at a monitoring point for each solution branch at $Ra = 4 \times 10^5$ (time scale is translated), we see that Branch 2 has the largest amplitude while Branch 4 is the smallest. The ratios between the squared amplitudes are in excellent agreement with those between the maxima of the deviations listed in Table III.

Although the above analysis explains the symmetry of the deviations of time-averaged solutions from the base solution observed at $Ra = 4 \times 10^5$ and the relationship between the deviations and the amplitudes of the corresponding periodic solutions, it is not clear why the spatial distributions of the deviations are almost the same for the three solution branches.

Copyright © 2002 John Wiley & Sons, Ltd.

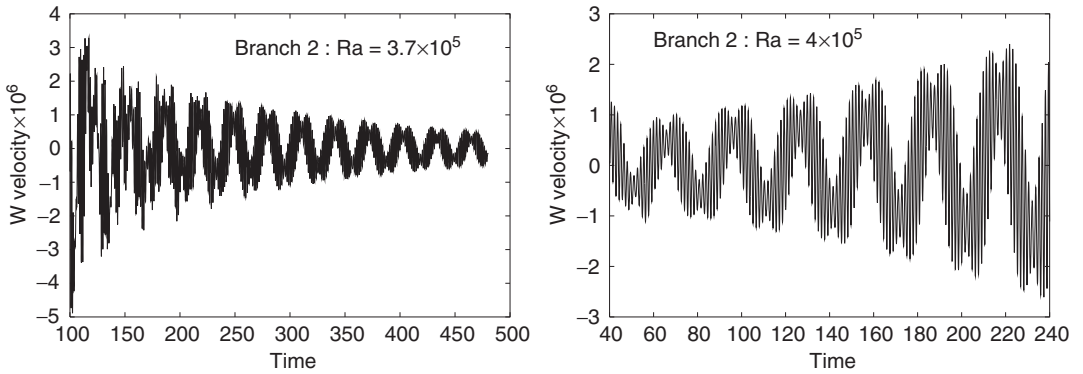

Figure 4. Time evolutions of w velocity component showing damped and amplifying 3D perturbations (Branch 2).

More efforts should be made in order to understand why and to study the link between the deviations and the stationary modes of the Jacobian.

3.4. *Two- to three-dimensional flow transition*

It is of course of some interest to investigate the validity of the two-dimensional assumption. We have investigated the stability of two-dimensional solutions to three-dimensional perturbations which are periodic in the third dimension. This was performed using time integration of the 3D equations described in Section 2.3, starting from either a steady 2D solution or a 2D unsteady solution. This was carried out with a spatial resolution of $32 \times 120 \times 40$ and we investigated disturbances of wavelengths comprised between 2 and 10. For subcritical Rayleigh numbers, i.e. steady 2D solutions, we did not find any unstable 3D perturbations. We then studied the mandatory Rayleigh number ($Ra = 3.4 \times 10^5$) and again did not find any unstable 3D perturbations. These results led us to the conclusion that up to $Ra = 3.4 \times 10^5$, the 2D solutions, either steady or unsteady, are stable to three-dimensional perturbations, although, as said earlier, these numerical investigations cannot be considered as a definitive proof.

In order to observe the 2D–3D transition, we investigated the stability of solutions on Branches 2, 3 and 4 for increasing Rayleigh numbers with a depth set at two times the cavity width. With increasing Ra Branch 2 was found to become 3D between 3.7×10^5 and 4×10^5 as three-dimensional perturbations are damped at $Ra = 3.7 \times 10^5$ and amplified at $Ra = 4 \times 10^5$ (Figure 4). Note that the cavity depth used which is equal to 2 times the cavity width is justified *a posteriori* by the fact that the corresponding flow structure contains only one wavelength in this direction (Plate 3). For Branch 3 the 2D-3D transition was located between $Ra = 3.8 \times 10^5$ and 4.2×10^5 while for Branch 4 the transition occurs between $Ra = 3.9 \times 10^5$ and $Ra = 4.5 \times 10^5$. It is worth noting that the 2D-3D transition is related to another Hopf bifurcation which results in a low frequency modulation even during linear phases. As the corresponding base solutions are periodic in time, there is no means to determine the critical points other than carrying out Floquet analysis [21, 22]. Fortunately the present periodic base solutions are two-dimensional and the third velocity component acts as perturbations. We can

Copyright © 2002 John Wiley & Sons, Ltd.

therefore measure growth rates during linear phase of the transients and estimate roughly the transition point for each branch by doing linear interpolation to find the root of $\sigma(Ra)=0$. The critical Rayleigh numbers obtained are equal to 3.84×10^5, 3.93×10^5 and 4.11×10^5, respectively, for Branches 2, 3 and 4. As we did not perform more computations to refine these critical values, they should still be considered as approximate.

The periods (angular frequencies) of the corresponding Hopf bifurcations were estimated from time evolutions of the third velocity component: it turned out that on each solution branch the travelling waves responsible for the 2D–3D transition have a longer period (lower angular frequency) than that of the periodic two-dimensional base flow. In order to understand the mechanism of the 2D–3D transition, we visualized the perturbations in various forms: isolines in constant x and z planes, isosurfaces, etc. We discovered that perturbations are mainly concentrated in the top and bottom thirds of the cavity and oscillate in the x–y plane. Plates 4, 5 and 6 show that perturbations consist of a weak travelling part along cavity walls and of a strong oscillating part in the core region: the oscillating part copes with the travelling part. As the 2D periodic base solution is independent of the z direction, the 2D–3D transition breaks this symmetry and perturbations responsible for that possess another symmetry of z-translation : $(\tilde{\theta},\tilde{u},\tilde{v},\tilde{w},\tilde{p})(x,y,z)=(\tilde{\theta},\tilde{u},\tilde{v},\tilde{w},\tilde{p})(x,y,z+D)$ where D is the cavity depth (period). This will be the symmetry of 3D perturbations on Branch 3 responsible for the 2D –3D transition due to the fact that the periodic base solution on Branch 3 does not possess any symmetry in the x–y plane. On the other hand the periodic base solutions on Branches 2 and 4 are symmetric in x–y plane, there exists a z_0 about which perturbations are either symmetric or anti-symmetric, i.e. $(\tilde{\theta},\tilde{u},\tilde{v},\tilde{w},\tilde{p})(x,y,z)=(-\tilde{\theta},-\tilde{u},-\tilde{v},\tilde{w},\tilde{p})(W-x,H-y,2z_0-z)$ or $(\tilde{\theta},\tilde{u},\tilde{v},\tilde{w},\tilde{p})(x,y,z)=(\tilde{\theta},\tilde{u},\tilde{v},-\tilde{w},-\tilde{p})(W-x,H-y,2z_0-z)$. Perturbations responsible for the 2D–3D transition on Branches 2 and 4 are therefore anti-symmetric.

Details of the 2D–3D transition such as critical Rayleigh number and critical wave number should be investigated in future through Floquet analysis along the lines of Reference [22].

4. SUMMARY AND CONCLUSIONS

In an air filled ($Pr=0.71$) differentially heated cavity of vertical aspect ratio 8 with adiabatic top and bottom walls, the transition from steady to time-dependent behaviour occurs at $Ra=306192\pm10$ and the critical angular frequency is equal to 1.709084. The corresponding perturbations (Mode 1) are travelling waves and break the symmetry of the steady base flow solution.

For the requested benchmark value of $Ra=3.4\times10^5$, the solution is periodic in time with a period of 3.4115 and symmetric in space. Visualization of the spatial structure of the fluctuations confirms that the solution results from the nonlinear saturation of the second most unstable mode (Mode 2) for which the critical parameters are $Ra_c=311170\pm10$ and $\mathscr{T}_c=3.424228$. Spatial and time resolution convergence were checked for the proposed reference solution.

Further computations show that the unsteady solution branch (Branch 1) corresponding to the most unstable eigenmode (Mode 1) exists only for a small range of Rayleigh number (up to $Ra=3.2\times10^5$). The supercritical regime was investigated up to $Ra=6\times10^5$, and four solution branches were obtained. Branch 2 extends approximately from $Ra=3.12\times10^5$ to $Ra=4.1\times10^5$, Branch 3 starts from $Ra=3.5\times10^5$ and Branch 4 begins at $Ra=4\times10^5$. The

Copyright © 2002 John Wiley & Sons, Ltd.

lower limit of Branch 3 agrees with the bifurcating point of Mode 3 which is $Ra_c = 333899.6$, Mode 3 is again symmetry-breaking. First appearance of quasi-periodic and chaotic flows are approximately observed at $Ra = 5.0 \times 10^5$ and $Ra = 5.4 \times 10^5$, respectively.

In the present work we were also interested in time-averaged solutions and especially in the difference between a time-averaged solution and the corresponding base flow solution. Particular attention is given to $Ra = 4 \times 10^5$ for which there are three periodic unsteady solutions. It turns out that the differences between the time-averaged solutions and the base solution are, to the norm of the eye, symmetric and have similar spatial distribution despite the fact that the periodic solutions result from different linearly unstable modes possessing different symmetries and angular frequencies. Asymptotic expansion explains at least why the differences are all seemingly symmetric and proportional to the amplitude squared of the periodic solutions. It would be of interest to investigate the relationship between the differences and the stationary modes of the Jacobian. We are deeply convinced that the answer to the question will shed light on our understanding of nonlinear interactions between different modes and contribute to the construction of low degree-of-freedom models for flow control.

Finally we investigated the stability of 2D solutions with respect to 3D perturbations. No 2D-3D transition occurs before the onset of time dependence of 2D flow nor at the mandatory *Ra* requested. By fixing a cavity depth equal to two times the cavity width we did observe 2D-3D transitions at higher Rayleigh numbers: the symmetry properties of the corresponding perturbations have been discussed and the critical *Ra* values were determined to be approximately equal to $3.84 \times 10^5, 3.93 \times 10^5$ and 4.11×10^5, respectively, for Branches 2, 3 and 4. These results show that the 2D assumption is marginally valid in the range of Rayleigh numbers corresponding to the transition to unsteadiness. More refined Floquet analysis should however be carried out.

In conclusion, we have addressed and assessed some of the issues concerning the computational predictability of natural convection in enclosures in the early unsteady and transitional regime, although more work is needed to extend these capabilities to real life (3D, complex geometries, variable properties) flow configurations.

ACKNOWLEDGEMENTS

The computations have been performed at Institut du Développement des Ressources en Informatique Scientifique (IDRIS) and Centre Informatique National de l'Enseignement Supérieur (CINES). The authors thank Dr E. Millour and Dr L.S. Tuckerman for invaluable discussions.

REFERENCES

1. Christon M, Gresho P, Sutton S. Computational Predictibility of Natural Convection Flows in Enclosures, *International Journal for Numerical Methods in Fluids* 2002; **40**:953–980.
2. Canuto C, Hussaini MY, Quarteroni A, Zang TA. *Spectral Methods in Fluid Dynamics*. Springer: New-York, 1988.
3. Bernardi C, Maday Y. Approximations spectrales de problèmes aux limites elliptiques. In *Collection Mathématiques Applications*, Ghidaglia JM, Lascaux P. (eds). Springer: Berlin, 1992.
4. Xin S, Le Quéré P. Linear stability analyses of natural convection flows in a differentially heated square cavity with conducting horizontal walls. *Physics of Fluids* 2001; **13**(9):2529–2542.
5. Le Quéré P. Etude de la transition à l'instationnarité des écoulements de convection naturelle en cavité verticale différentiellement chauffée par méthodes spetrales Chebyshev. *Thèse d'Etat*, Univ. de Poitiers, 1987.
6. Vanel JM, Peyret R, Bontoux P. In: *Numerical Methods for Fluid Dynamics*, vol. II, Morton KW, Baines MJ. (eds). Clarendon Press, Oxford, 1986, 463–475.

Copyright © 2002 John Wiley & Sons, Ltd.

7. Gresho PM, Sani RL. Advection–Diffusion and Isothermal Laminar Flow. *Incompressible Flow and the Finite Element Method*, vol. 1. Wiley: New York, 2002.
8. Kleiser L, Schumann U. Treatment of incompressibility and boundary conditions in three-dimensional numerical spectral simulations of plane channel flows. *Notes in Numerical and Fluid Mechanics*, Vieweg, 1980; **2**: 165–173.
9. Tuckerman LS. Divergence-free velocity fields in nonperiodic geometries. *Journal of Computational Physics* 1989; **80**(2):402–441.
10. Le Quéré P. An improved Chebyshev collocation algorithm for the direct simulation of chaotic flows in differentially heated cavities. *Finite Elements in Analysis and Design* 1994; **16**:291–283.
11. Saad Y, Schultz M. GMRES: a generalized minimal residual algorithm for solving nonsymmetric linear system. *SIAM Journal of Science and Statistical Computing* 1986; **7**:856–869.
12. Mamun CK, Tuckerman LS. Asymmetry and Hopf bifurcation in spherical Couette flow. *Physics of Fluids* 1995; **7**(1):80–91.
13. Chenier E. Etude de la stabilité linéaire des écoulements thermocapillaires et thermogravitationnels en croissance cristaline. *Thése de Doctorat*, Univ. Paris Sud (1997).
14. Xin S, Le Quéré P, Daube O. Natural convection in a differentially heated horizontal cylinder: effects of Prandtl number on flow structure and instability. *Physics of Fluids* 1997; **9**(4):1014–1033.
15. Tuckerman LS, Barkley D. *Bifurcation Analysis for Timesteppers*, vol. 119. The IMA, Springer: Berlin, 2000; 453–466.
16. Griewank A, Reddien G. The calculation of Hopf points by a direct method. *Journal of Analysis* 1983; **3**: 295–303.
17. Winters KH. Hopf bifurcation in the double glazing problem with conducting boundaries. *Journal of Heat Transfer* 1987; **109**:894–898.
18. Bergeon A, Henry D, Benhadid H, Tuckerman LS. Marangoni convection in binary mixtures with Soret effect. *Journal of Fluid Mechanics* 1998; **375**:143–177.
19. Achdou Y, Guermond J.-L. Convergence analysis of a finite element projection/Lagrange-Galerkin method for the incompressible Navier–Stokes equations. *SIAM Journal of Numerical Analysis* 2000; **37**:799–826.
20. Le Quéré P. Onset of unsteadiness, routes to chaos and simulations of chaotic flows in cavities heated from the side: a review of present status. *Proceedings of the 10th IHTC Conference*, GK8, vol. 1. Hemisphere Publishing C.: Washington, DC, 1994; 281–296.
21. Iooss G, Joseph DD. *Elementary Stability and Bifurcation Theory*. Springer: Berlin, 1980.
22. Barkley D, Henderson R. 1996, Three-dimensional Floquet stability analysis of the wake of a circular cylinder. *Journal of Fluid Mechanics* 1996; **322**:215–241.

Copyright © 2002 John Wiley & Sons, Ltd.

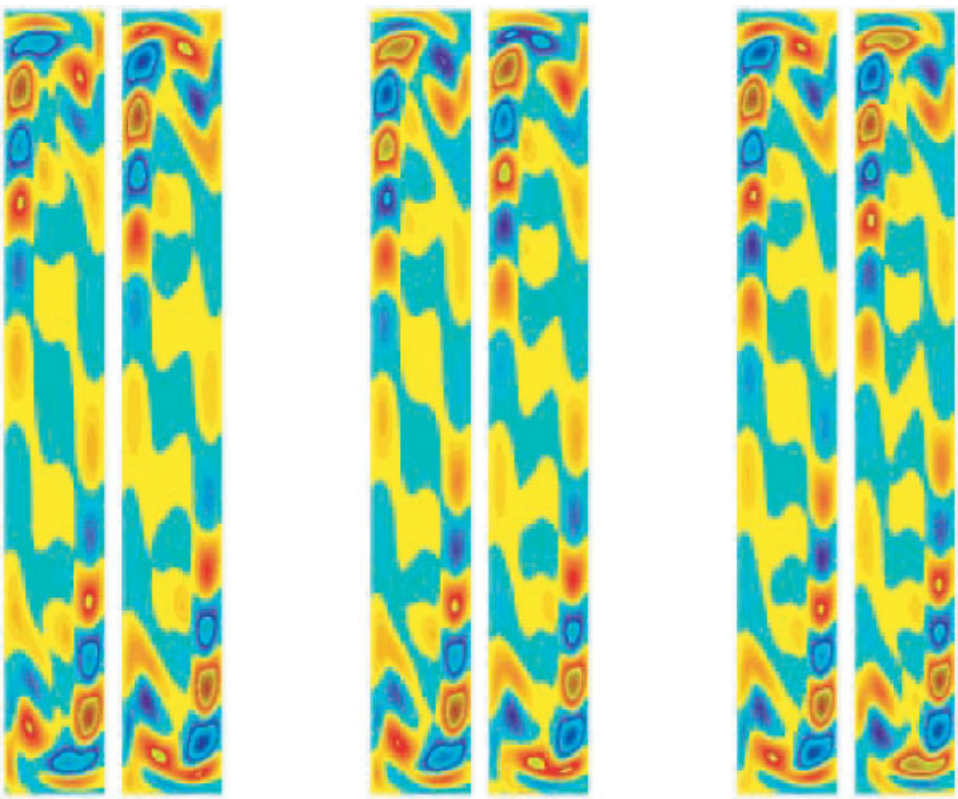

Plate 1. Real and imaginary parts of temperature eigenmodes of the first three most unstable modes. Mode 1 (left), Mode 2 (middle) and Mode 3 (right).

Copyright © 2002 John Wiley & Sons, Ltd.

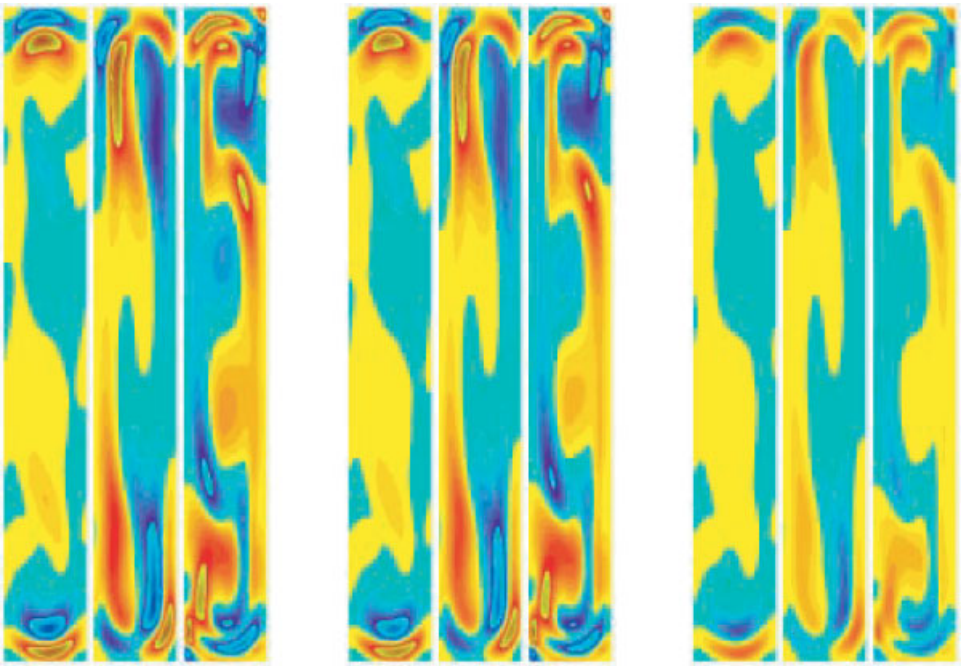

Plate 2. Differences between time-averaged and unstable base solution at $Ra = 4 \times 10^5$ (Branch 2: left, Branch 3: middle, Branch 4: right). The fields are shown in u, v and θ order.

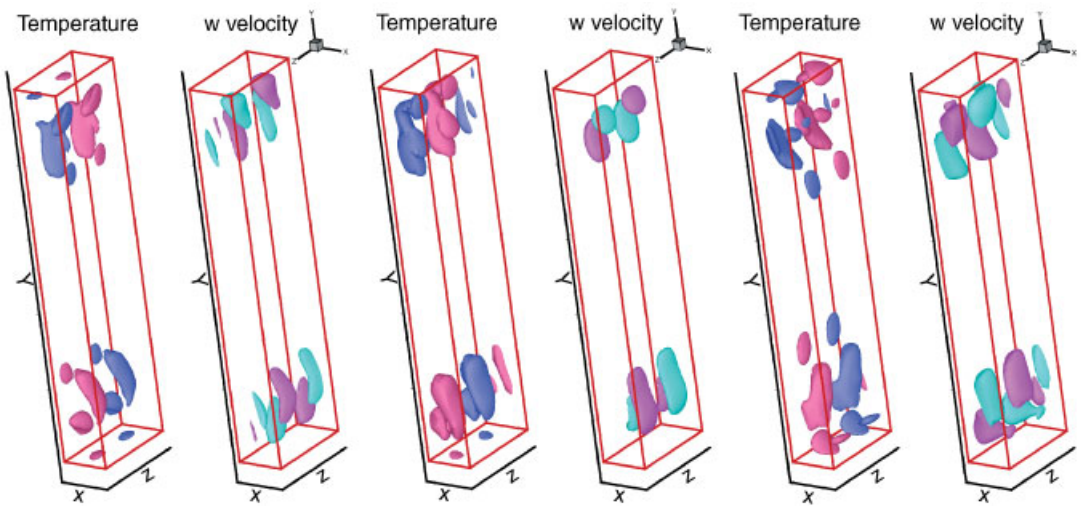

Plate 3. Spatial distribution of 3D disturbances (from left to right: Branch 2, Branch 3 and Branch 4).

Copyright © 2002 John Wiley & Sons, Ltd.

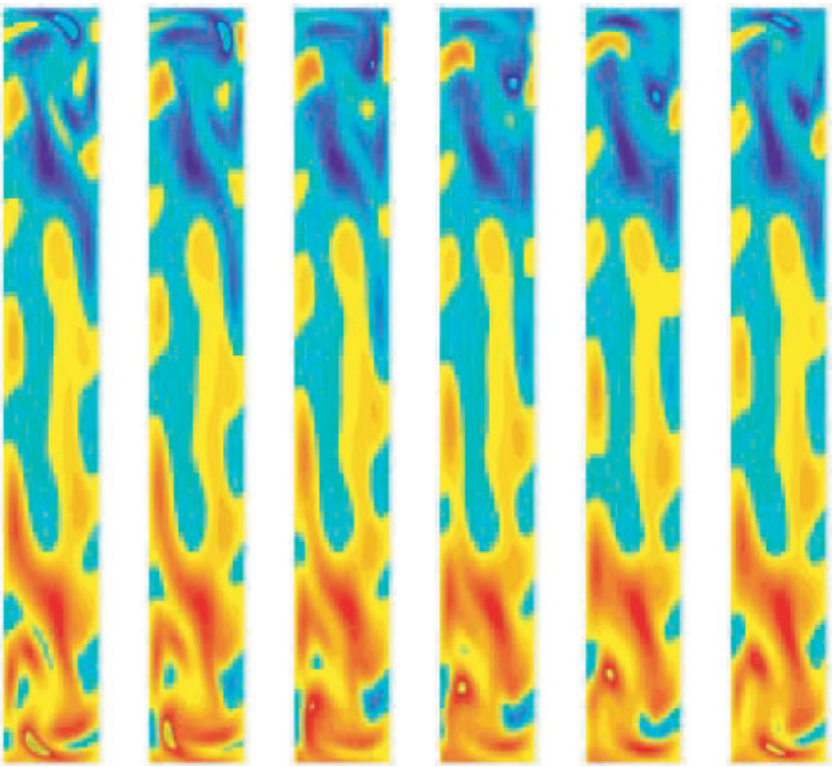

Plate 4. Temperature perturbations of the unstable oscillatory 3D mode at $Ra = 3.9 \times 10^5$ (Branch 2).

Copyright © 2002 John Wiley & Sons, Ltd.

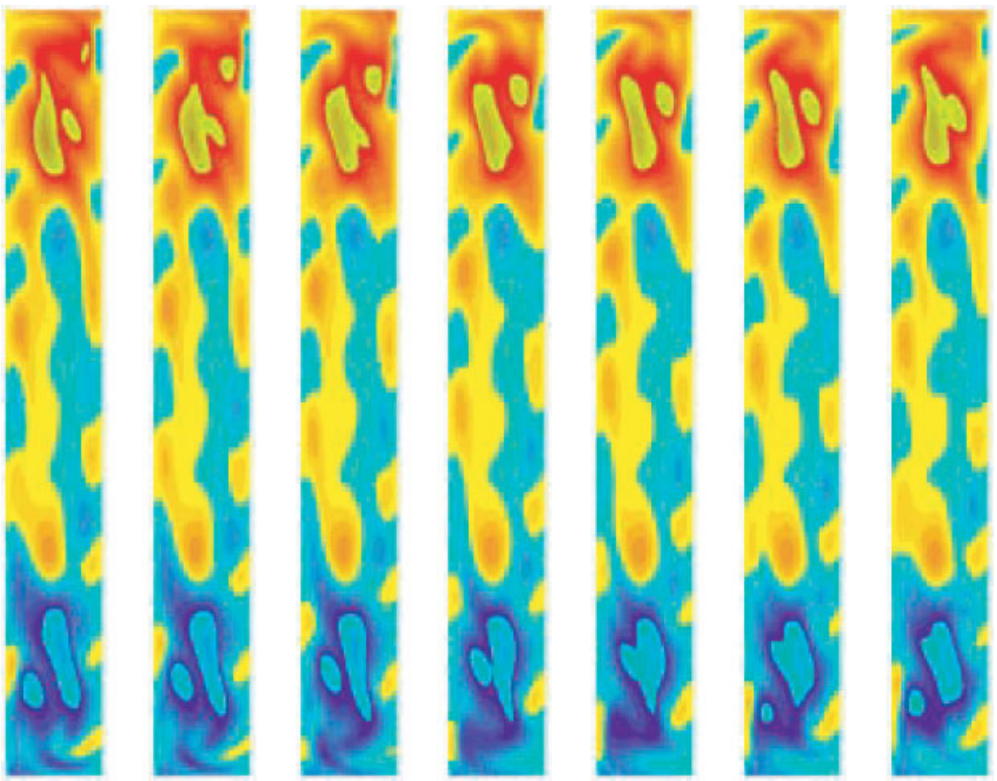

Plate 5. Temperature perturbations of the unstable oscillatory 3D mode at $Ra = 3.9 \times 10^5$ (Branch 3).

Copyright © 2002 John Wiley & Sons, Ltd.

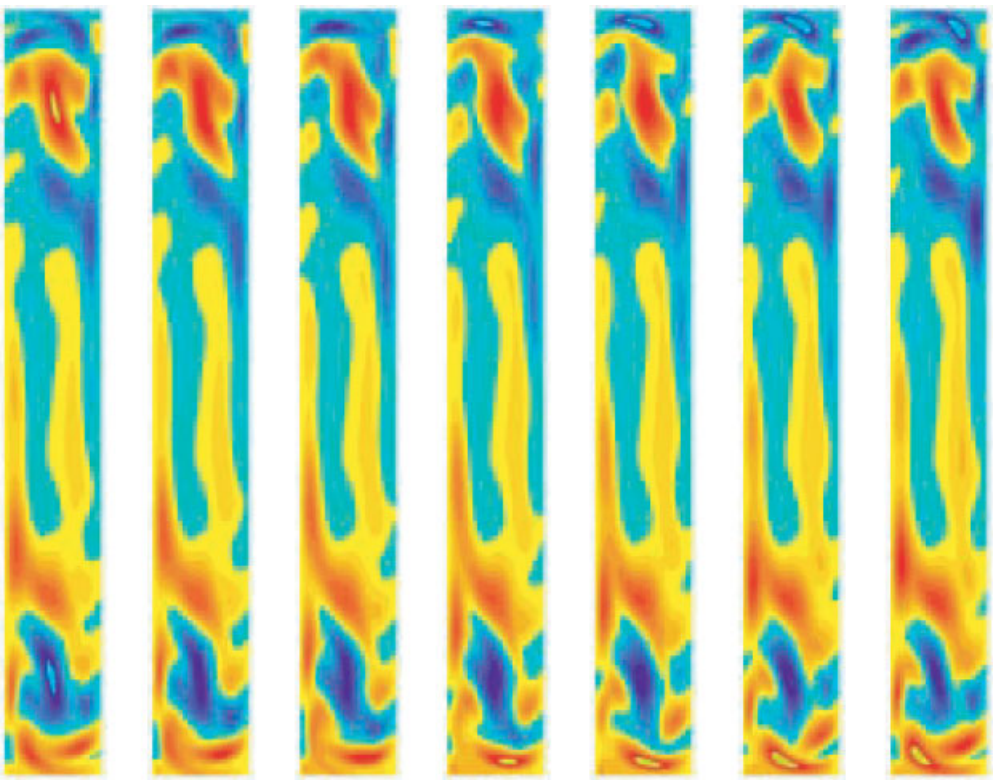

Plate 6. Temperature perturbations of the unstable oscillatory 3D mode at $Ra = 3.9 \times 10^5$ (Branch 4).

Copyright © 2002 John Wiley & Sons, Ltd.